Depth quantification of surface-breaking cracks in ferromagnetic materials using DC-biased magnetization based induction thermography

Jianbo Wu[a], Junzhen Zhu [a,b,c,*], and Gui Yun Tian[b]

[a] *School of Mechanical Engineering, Sichuan University, Chengdu, China;*

[b] *School of Engineering, Newcastle University, Newcastle upon Tyne, UK;*

[c] *Department of Vehicle Engineering, Army Academy of Armored Forces, Beijing, China;*

Corresponding author: j.zhu11@ncl.ac.uk

Depth quantification of surface-breaking cracks in ferromagnetic materials using DC-biased magnetization based induction thermography

Abstract: A common challenge in maintenance of critical structures is how to fast localize and quantify geometries of surface-breaking cracks. Induction thermography (IT) is a potential technique to detect this type of defects. However, for testing ferromagnetic structures, if a deep defect exists in the wall structure, only its shallower part within the skin-depth layer affects the early thermal response of IT, whereas its deeper part hardly has any influence on the early response. To extend the detectable depth range of traditional IT for ferromagnetic materials, a DC-biased magnetization based induction thermography (DCMIT) technique is introduced in this paper. Based on the permeability distortion in the skin-depth layer, DCMIT can build a monotonic relation between the thermal feature and the defect depth. Results show that when the coil direction is parallel to the notch's length direction, DCMIT can quantify the notch with a depth up to 6.0 mm whereas traditional IT can hardly achieve this depth detection.

Keywords: Surface-breaking cracks; stress corrosion cracking; induction thermography; DC-biased magnetization; depth quantification

1. Introduction

Stress corrosion cracking (SCC) is a common hazard threatening the structural integrity in many industries [1-5], e.g., oil, gas, nuclear power, automotive, marine, etc. SCC is induced from the combined influences of corrosive working environments and high tensile stresses. Failures caused by SCC can be unexpected and catastrophic. Thus, detecting and evaluating SCC at the initiation stage is one of the most important issues to protect critical components from impacts of SCC. Stress corrosion cracks commonly exist in the outer and inner surfaces of wall structures which belong to one typical type of surface-breaking cracks [6]. Nowadays, various nondestructive testing (NDT) techniques with individual advantages have been developed to detect surface-breaking cracks, e.g., ultrasonic testing [7-11], X-ray tomography [12-13], current field perturbation techniques (eddy current testing [14-16], alternating current potential drop [17], alternating current field measurement [18-20]), magnetic flux leakage testing [21]. As a promising candidate, induction thermography (IT), a.k.a. eddy current thermography and electromagnetic thermography, is a multi-physics-based technique for fast crack detection and quantification [22-24]. The working principle of IT is that a defect within the effective skin depth diverts current paths, which results in an uneven current density and then contributes to an abnormal thermal distribution.

Apart from evaluating various critical components [25-28], for detecting surface-breaking cracks in metallic materials by using IT technique, many case studies have been conducted in recent years. Oswald-Tranta et al. [29] investigate how to localize shallow cracks in castings using gradients and second derivatives of phase images. They also introduce an IT configuration with two Helmholtz coils perpendicularly arranged to eliminate the crack orientation dependency on thermal responses. Additionally, they use phase contrasts under a single pulse [30] or SNR-enhancing multiple pulses [31] to quantify depths and angles of surface-breaking cracks. Wang et al. [32], by combining optical flow and principal component analysis, extract thermal patterns to localize micro cracks in driven key, which is a critical part of the aircraft braking system. Xu et al. [33] reconstructe crack shapes in a polycrystalline diamond compact bit by utilizing principal

component analysis and image stitching. Wang et al. [34] investigate the effect of coating layers on surface crack detection.

However, IT inevitably faces two major limitations. One problem is that during fast testing in the early heating stage, the thin skin depth of the ferromagnetic material contributes to a shallow and concentrated Ohmic heating layer [35]. If a deep defect exists, only the shallower part has a strong link with Ohmic heating and the deeper part almost has no influence on it. This situation limits IT's capability of quantifying depth information. Additionally, detectability of defects highly depends on the coil-defect direction and the most challenging case is that the coil direction is parallel to the defect's length direction [29]. Focusing on these two limitations, this paper achieves defect detection and depth quantification via the previously proposed DCMIT technique [36]. Different from previous work (detection of deep subsurface defects), this work tries to build a monotonic relation between the enhanced thermal feature and the depth of the surface-breaking defect, which relies on the nonlinear μ-H relation and the permeability distortion in the skin-depth layer. The remaining sections are structured as: the fundamentals of IT and DCMIT are introduced and compared in Section 2; the study diagram of depth quantification using DCMIT is presented in Section 3; Section 4 experimentally studies the effect of DCMIT on defect detection. This section also compares the performances of DCMIT and IT for depth quantification; the conclusion and future work are given in Section 5.

2. Theoretical fundamentals

2.1. Fundamentals of IT

The thermal diffusion process with a time-invariant induction heating source can be represented as [37]

$$\lambda \nabla^2 T - \rho C_p \frac{\partial T}{\partial t} = -q \tag{1}$$

where, λ, ρ, C_p are the thermal conductivity, density, and thermal capacity, respectively. $\nabla^2 T$ means the divergence of the thermal gradient. And q denotes the heating power per unit volume, which includes hysteresis losses (proportional to frequency f), classical eddy current losses (proportional to f^2), and excess losses (proportional to $f^{3/2}$) considering ferromagnetic materials [38].

For the frequency about 280 kHz used in this study, the classical losses become the dominant heating source. It is considered with the following relation [39]

$$q \sim I_{coil}^2 \sqrt{\frac{\mu f_{coil}}{\sigma}} \tag{2}$$

where, I_{coil} and f_{coil} are the RMS value and the frequency of the AC current through the coil, respectively. μ denotes the permeability and σ is the electrical conductivity.

Eq. (2) shows that under a constant excitation frequency any μ- or σ-distortion caused by defects will affect the eddy current/Ohmic heating power and further result in abnormal thermal distributions. Fig. 1(a) schematically gives the μ distribution in a defective specimen without DC-biased magnetization (DCM). It shows that without any DCM, the μ distribution doesn't change, which is shown in dark blue. Then, if AC excitation is introduced, i.e. IT is used, the effective μ distribution can only vary within a narrow working range, which is denoted as 'μ-IT' in Fig. 1(c). The heating power (q) is mainly dominated by the σ-distortion and two tips (A and B) of the notch generate much stronger Ohmic heating. Based on this phenomenon, the relevant thermal features can be

used to quantify different defect lengths/depths. However, if a surface-breaking defect has a deep depth, IT cannot easily quantify its depth. It is because that most of the induced eddy current distributes within the skin-depth layer. If a deep defect exists, only the shallower part within the skin-depth layer affects the eddy current distribution and the deeper part almost has no influence on it. This leads to the nonlinear relation between the thermal feature and the defect depth [40]. It is especially true for ferromagnetic materials because of their high electrical conductivity and permeability.

2.2. Fundamentals of DCMIT

In the aforementioned section, it is challenging for IT to quantify the depth of a deep defect. Here, a permeability-distortion-based method, i.e. DCMIT, is introduced to address this issue. The *B*-*H* relation is [41]

$$\vec{B} = \mu_0 \mu_r \vec{H} = \mu \vec{H} \tag{3}$$

where, $\vec{B}$ and $\vec{H}$ are the magnetic induction and the magnetic field. μ_0 and μ_r are the magnetic constant and relative permeability.

For ferromagnetic materials, the *B*-*H* or μ-*H* relation is highly hysteretic. Typical *B*-*H* and μ-*H* curves of the AISI 1045 carbon steel is shown in Fig. 1(c). From this curve, when *H* is strong (under DC-biased magnetization), μ has a nonlinear and inverse relation with *H*. If a defect exists, it will affect its surrounding magnetic flux and distort the μ distribution, as shown in Fig. 1(b). The μ distributions of all the four vicinities (*A*, *B*, *C*, and *D*) around the defect are distorted. In the two tips (*A* and *B*), the permeability (in dark blue) is lower than the sound/background permeability (in light blue). Instead, in the other two vicinities (*C* and *D*) along the length direction, the permeability (in orange) is higher than the background permeability. Based on Eq. (2), it is obvious that the heating powers in *C* and *D* are higher than those in the two tips. Note that in this work DC-biased magnetization plays a leading role in affecting the permeability compared with AC induction. Thus, we assume that the effective μ distributions result from DC magnetization, as shown by 'μ-DCMIT' in Fig. 1(c), without much considering the minor AC hysteresis loop [42].

From the above descriptions, the heating power distributions/patterns of IT and DCMIT are different. For IT, most of the heating powers exist at the two tips of the notch, whereas DCMIT locates the heating powers along the edges of the notch. This difference occurs because of different permeability working ranges. IT works in an initial and narrow permeability range ('μ-IT' in Fig. 1(c)) whereas DCMIT can work in a much wider permeability range ('μ-DCMIT'). The main advantage of DCMIT is utilizing the permeability distortion in the skin-depth layer. And even if a defect has a very deep depth, this permeability distortion still has a strong link to the depth. Then, the corresponding abnormal thermal distributions can be achieved in the early heating stage. The detailed and quantitative results will be discussed in Section 4.2.

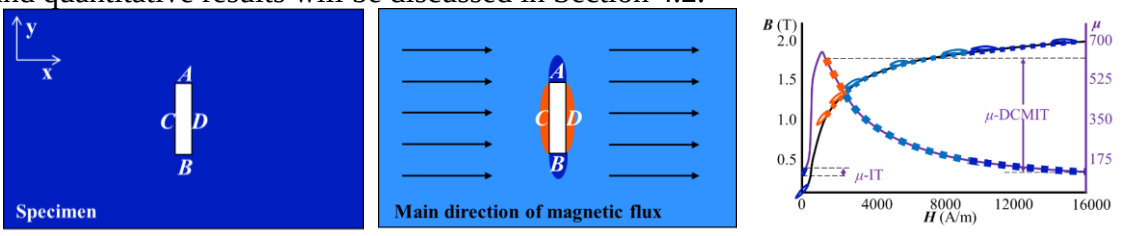

(a) (b) (c)

Fig. 1. Schematic μ distributions without and with DCM. (a) Without DCM. (b) With DCM. (c) Typical *B*-*H* and μ-*H* curves of AISI 1045 carbon steel [43]. Note that μ denotes the relative permeability.

3. Study diagram

Fig. 2 shows the study diagram for defect depth quantification using DCMIT. It starts with building DCMIT configuration by setting the excitation parameters, choosing the coil type, and configuring the DC-biased magnetizer. Later, thermal video preprocessing is conducted by cropping the region of interest (ROI) and the background subtraction. Two specific studies are then investigated: the effect of DCMIT on defect detection and the thermal peak (T_p) used for depth quantification. Further, two criteria, i.e. the coefficient of determination (R^2) and the norm of residuals ($\|e\|$), are used to compare and evaluate the performance of T_p for the defect depth quantification.

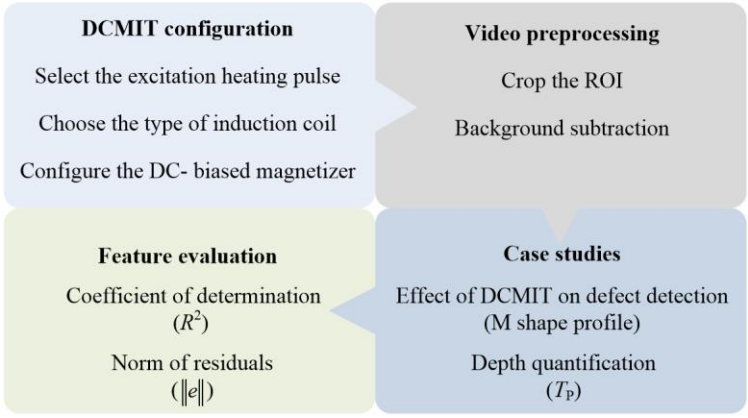

Fig. 2. Proposed study diagram of this work.

4. Experimental studies

According to the study diagram in Fig. 2, the following sections discuss the detailed experimental studies.

4.1. DCMIT configuration and specimens

Fig. 3 shows the DCMIT configuration used for experiments. Three main units constitute the whole configuration, i.e. an induction heating module with a rectangle coil, an infrared camera, and a DC-biased magnetizer (including a DC power supply, a magnetizing coil, and a U-shape yoke). The specific units and parameters used in this study are the same as them used in [36], e.g., types of the heating module and the infrared camera, the induction frequency (285 kHz), intensity (380 A) and duration (50 ms), the frame rate (200 Hz) and resolution of the infrared camera (640×120 pixels), etc.

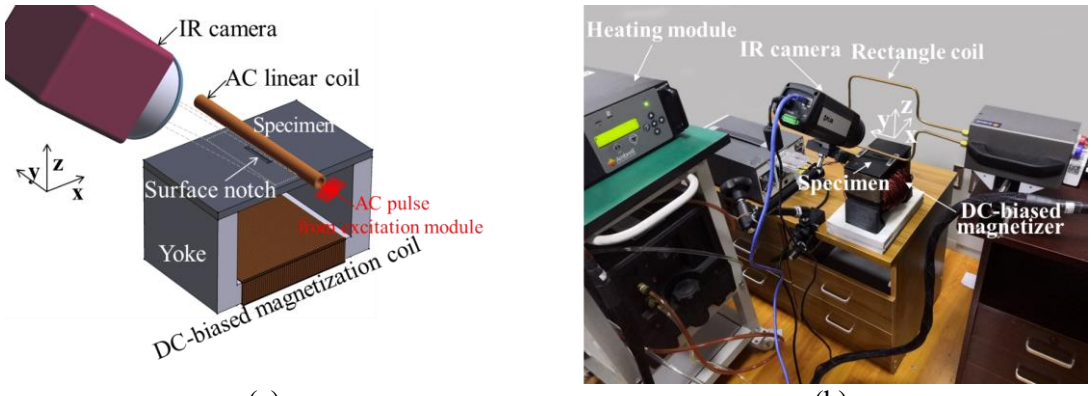

(a) (b)

Fig. 3. DCMIT configuration. (a) Schematic DCMIT configuration. (b) Full view of DCMIT configuration.

For simulating simplified stress corrosion cracks, six plates made of AISI 1045 carbon steel were milled with artificial notches in the middle, as shown in Fig. 4. All plates have the same dimension of (160 × 100 × 7) mm^3. The notches have the same length and width of 30.0 mm and 4.0 mm, respectively. But the depths (d) vary from 1.0 to 6.0 mm with a 1.0 mm interval. To increase the surface emissivity to around 0.9 [44], all the plates were covered with the matt black paint. A 5.0 mm lift-off distance between the coil and the specimens is controlled by two glass blocks having the same 5.0 mm thickness, as shown in Fig. 3(b).

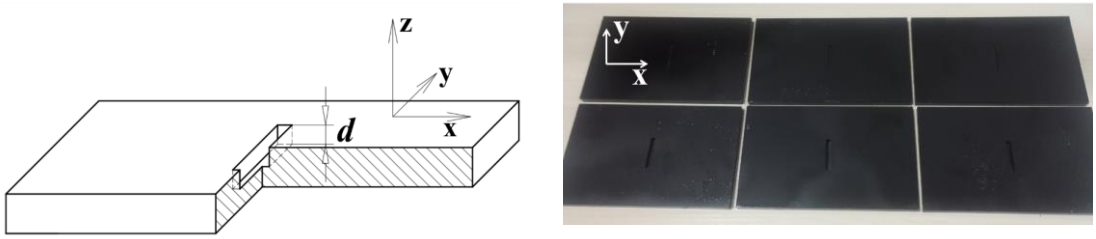

(a) (b)

Fig. 4. Specimens used in experiments. (a) Partial section view the specimen. (b) Photo of the specimens (blackened).

4.2. Effect of DCMIT on defect detection

In prior work, the optimal direction of the DC-biased magnetization having the strongest correlation to the thermal response is found when the DC magnetization direction is in line with the AC magnetization direction of the coil [36], as shown in Fig. 3. Thus, this direction is used for investigating the effect of DCMIT on defect detection. For simplification, in the following sections the direction and the current value of DC-biased magnetization are denoted by M_{DC} and I_{DC}, respectively.

Figs. 5(a)-(c) show the thermal distributions of the notch vicinities under six different I_{DC}. The depths of these surface notches are 1.0, 4.0 and 6.0 mm, respectively. Comparing the subfigures in Fig. 5(a), (b) or (c), if I_{DC} is zero (equal to traditional IT), both the left and right tips of the notch have higher thermal responses than those of the top and bottom sides. When I_{DC} increases, the above founding changes to the opposite situation, i.e. the top and bottom sides have higher thermal responses. This change is more obvious for a deep notch with the I_{DC} increasing from 0 to 20 A, as shown in Fig. 5(c). All these results are in line with the fundamentals discussed in Section 2.2.

Further, Figs. 5(d)-(f) show the line plots (l_1) across the middle of each notch. All the line plots show clear 'M' shape profiles. The two peaks (T_{PU} and T_{PD}) of the 'M' profile represent the maximum thermal responses of both top and bottom sides of the notch. In Fig. 5(d), for the notch with 1.0 mm depth, both T_{PU} and T_{PD} decrease with I_{DC} increasing. However, in Fig. 5(e) for the notch with the 4.0 mm depth, T_{PU} and T_{PD} increase initially, then reach their maximum values (around 4.2 ℃), and decrease afterwards when the I_{DC} increases from 4 to 20 A. In Fig. 5(f) for the notch with the 6.0 mm depth, T_{PU} and T_{PD} monotonically increase with I_{DC}, and T_{PU} and T_{PD} reach the maximum values (around 4.7 ℃) when I_{DC} is 20 A. It is noteworthy that the relations between T_{PU} (or T_{PD}) and I_{DC} present different trends. These trends mainly result from varied patterns of the permeability distortion by different notch depths. The line plots from experimental data show the surface thermal distributions but cannot directly present the permeability distributions. In the following, a 3D numerical model based on finite element method is built to directly show the permeability distortion and investigate the relation between the permeability distortion and T_{PU} (or T_{PD}).

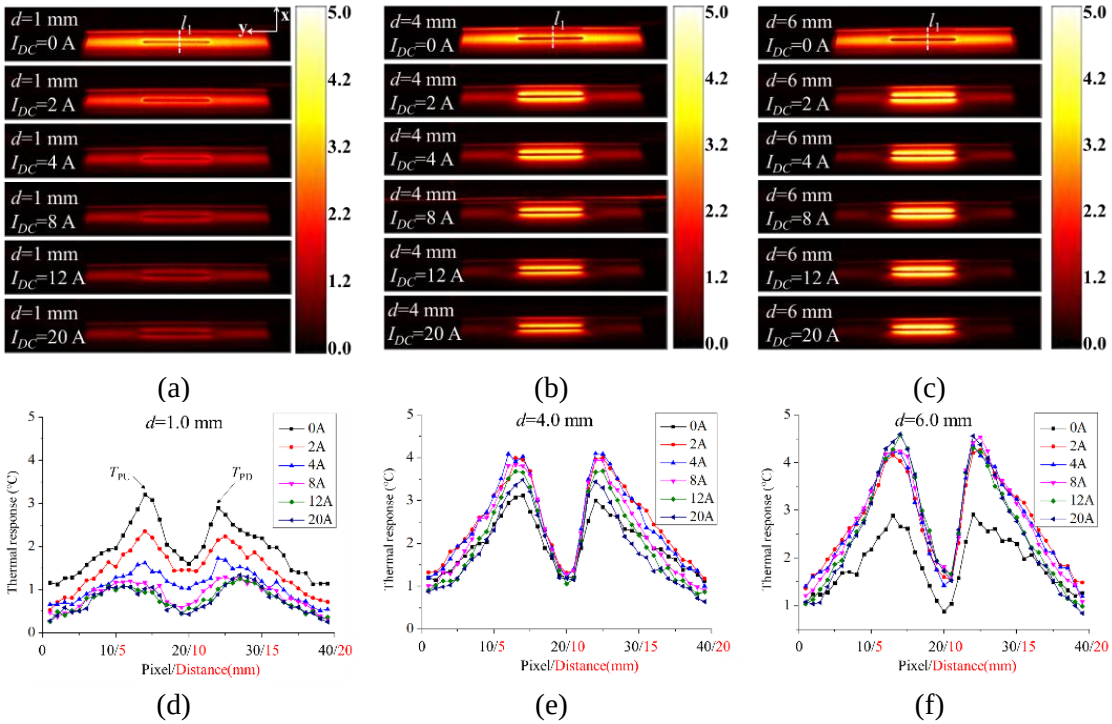

Fig. 5. Surface thermal distributions of the notches with three depths and the line (l_1) profiles under six I_{DC} values. (a), (b), and (c) give the thermal distributions around the notch vicinity after a 50 ms heating pulse under six different I_{DC}, respectively. l_1 is vertical to the notch's length and goes across the middle of each notch. (d), (e), and (f) show the line profiles of thermal responses along l_1 under six different I_{DC}, respectively.

Fig. 6 shows the FEM model used and the simulation results. COMSOL Multiphysics with the magnetic field interface is used. As mentioned in Section 2.2, DC-biased magnetization has the major contribution to μ distributions in the specimen. Therefore, this FEM model is simplified without considering the induction heating and the heat diffusion process, as shown in Fig. 6(a). After meshing, this model consists of 1,060,958 elements with a 0.71 averaging quality. All the geometric and material parameters are the same as the experimental studies'. Here, a surface notch with a 4.0 mm depth is shown as an example. A cross-section plane vertical to the length direction of the notch is selected to further investigate the magnetic flux density and the permeability distribution.

After computing, Fig. 6(b) shows the norm of magnetic flux density (top view) under 10 A I_{DC} when d is 1, 4, and 6 mm, respectively. It shows that the magnetic flux density values at the slot tips are higher, whereas they are lower along the slot length direction. Since we are more interested in the permeability changing, based on the constitutive relation of B-H, Fig. 6(c) gives the permeability distribution. Conversely, it clearly shows that the permeability values along the notch's length direction are much higher than that of sound areas, whereas they are much lower around the tips. Figs. 6(d) and (e) further show the cross-section view of B and μ distributions, respectively. In Fig. 6(e), the permeability values through the notch depth are distorted and much higher than that of other areas. To investigate the near-surface permeability distortion, a line (l_2) within the skin-depth layer and parallel to the top surface is plotted.

Fig. 6(f) shows the relative permeability (μ_r) values along l_2 of different notch depths. To better describe the permeability change, two horizontal distances (Z_0 and Z_1) are given in this figure. Z_0 shows notch width or the air gap distance (4.0 mm) and Z_1 gives a 3.0 mm distance away from both sides of the notch. By comparing Fig. 6(f) with Figs. 5(d)-(f), the μ_r profiles along l_2 are similar to the thermal profiles along l_1 but a difference exists

in the middle part. In the μ_r profile, the values change very sharp and all the values in Z_0 come to one, whereas the values of thermal profile decrease from two peaks to the middle trough is relatively gentle. The reason resulting in this difference is that the heat propagation process exists in the experimental studies and it diffuses the heat distribution. Still, the heat diffusion has a limited influence on the link between the permeability distortion and the thermal peaks (T_{PU} and T_{PD}) since the heating pulse is just 50 ms. Additionally, Fig. 6(f) indicates that μ_r in Z_1 increases with the notch depth. An example is shown by comparing the shaded area under the curve of 1mm with the area of 2 mm. Thus, a monotonic relation between the μ_r and notch depth can be obtained by using a larger I_{DC}. In the next section, the detailed relations between the thermal peak and the notch depth under different I_{DC} are experimentally compared and the optimal relation is found to quantify the notch depth.

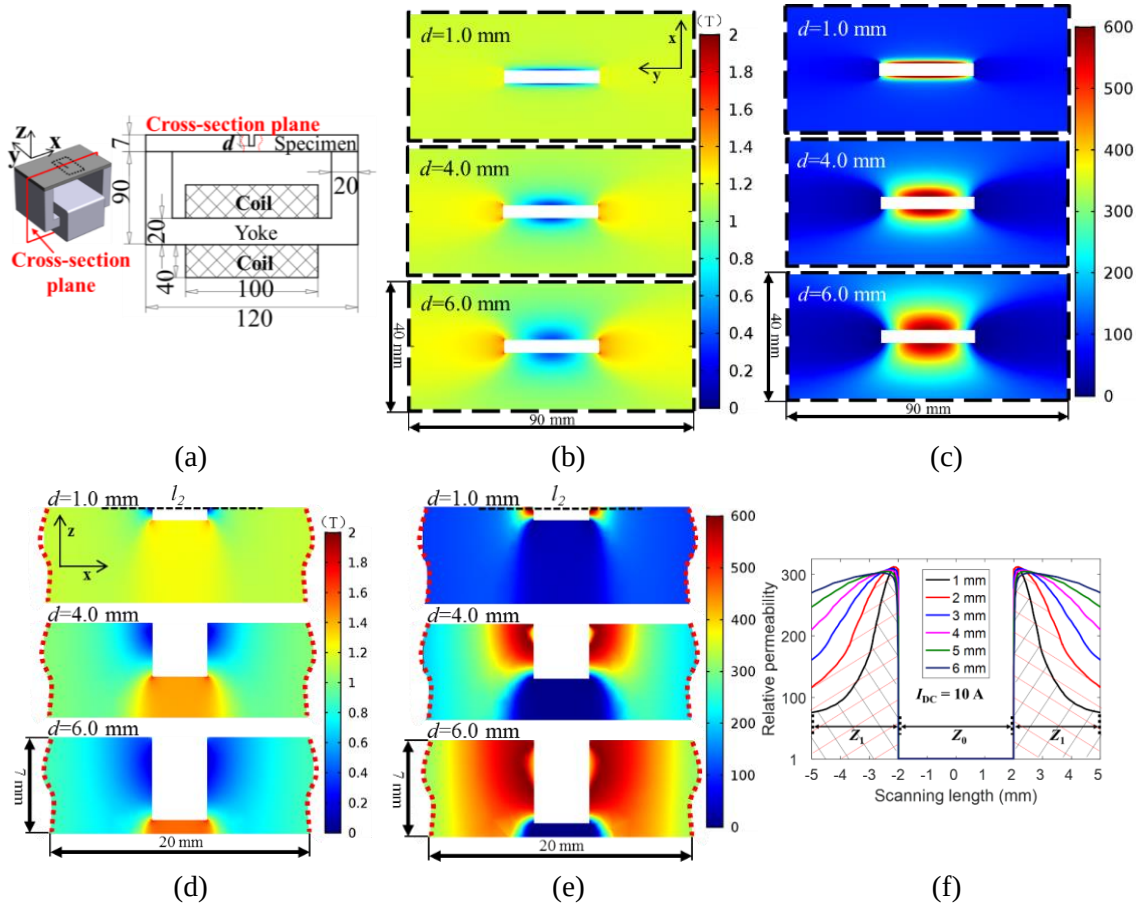

Fig. 6. 3D model for FEM simulation and calculation results. (a) 3D model with a notch (left). A cross-section plane vertical to the notch's length direction is also plotted (right). (b) Top view of magnetic flux density norm distributions when I_{DC} is 10 A and the notch depth is 1.0, 4.0 and 6.0 mm, respectively. l_2 has a length of 20 mm and its vertical distance to the top surface is 10 μm. (c) Top view of permeability distributions. (d) and (e) are the cross-section view of magnetic flux density norm and permeability distributions, respectively. (f) further shows the value of μ_r along l_2 when the notch depth changes from 1.0 to 6.0 mm.

4.3. DCMIT for defect depth quantification

Fig. 7 shows the capabilities of traditional IT and DCMIT for quantifying the notches with different depths. By comparing Fig. 7(a) with (c), IT (I_{DC} is zero) can only show the tips of the notches but hardly show any thermal difference with the depth changing. In contrast, DCMIT can easily present different thermal responses with the depth increasing.

The line plots in Figs.7 (d)-(f) further illustrate the above results. Fig. 7(d) shows that the thermal responses are almost the same with the depth changing. This means that in this study IT cannot be properly used for depth quantification. Additionally, comparing Fig. 7(e) with (f), the enhanced thermal difference with varying depths can be achieved by increasing I_{DC}.

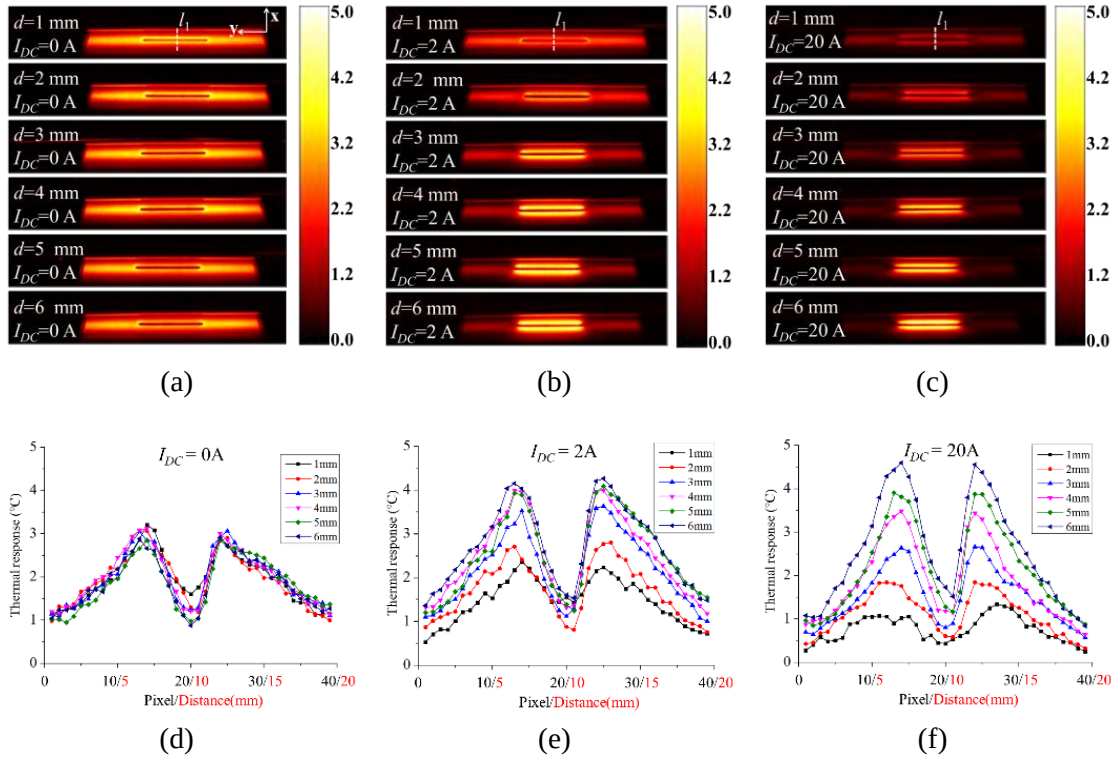

Fig. 7. Results comparison of IT and DCMIT. (a), (b), and (c) give the thermal distributions around the notch vicinity after a 50 ms heating pulse by using IT (without I_{DC}) and DCMIT (2A and 20A I_{DC}), respectively. The depth of each surface-breaking notch ranges from 1.0 to 6.0 mm. (d), (e), and (f) show the line profiles of thermal responses along l_1 by using IT and DCMIT, respectively.

Fig. 8 shows the detailed comparative results when using IT and DCMIT to quantify the notch depth. Here, the peak value T_P (the average of T_{PU} and T_{PD}) is used as the thermal feature. In Fig. 8(a), when I_{DC} is zero, T_P values are overlapped with notch depth changing from 1.0 to 6.0 mm. It means that the peak value from IT cannot be used to build a monotonic relation with notch depth when the coil direction is parallel to the notch's length direction. With I_{DC} increasing, the differences between T_P values of varied depths increase. This clearly shows that T_P from DCMIT (by using a larger I_{DC}) can build a monotonic relation with notch depth. This figure also shows that T_P of 1.0 and 2.0 mm notch depths have a decreasing trend with I_{DC} increasing. T_P of 3.0, 4.0, and 5.0 mm notch depths first increase and then decrease with I_{DC} increasing. And T_P of 6.0 mm notch depth has an increasing trend with I_{DC}. The three different trends are in line with the results from Figs. 5(d)-(f). Additionally, Fig. 8(b) shows the quadratic fitting plots between T_P and the notch depth under different I_{DC} values. Table 1 gives the assessing parameters, i.e. coefficient of determination (R^2) and norm of all the residuals ($\|e\|$), of each fitting plot in Fig. 8(b). It shows that with I_{DC} increasing, the R^2 increases and $\|e\|$ decreases. When I_{DC} is 20 A, R^2 and $\|e\|$ reach to 99.7 % and 0.37 which present the best quadratic fitting relation between T_P and the notch depth.

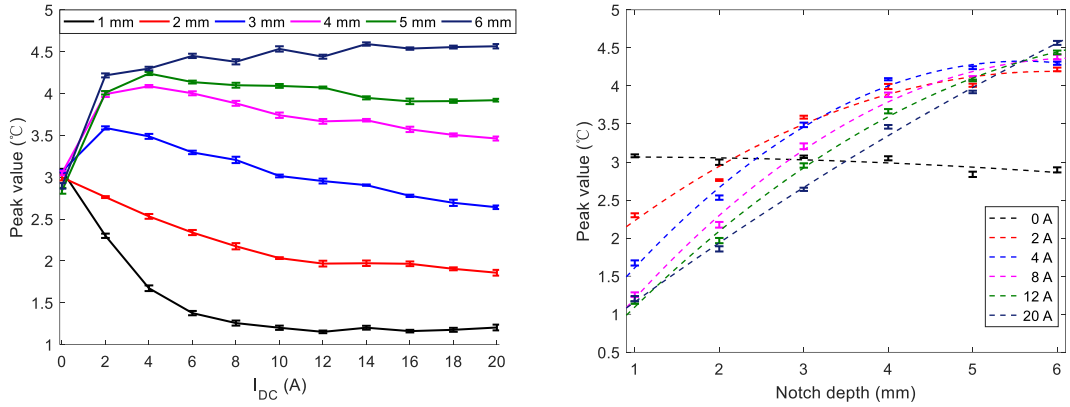

(a) (b)

Fig. 8. Relations between T_P and I_{DC} and notch depth. (a) T_P vs. I_{DC}. (b) T_P vs. notch depth with quadratic fitting lines.

Table 1. Coefficient of determination and norm of all the residuals of fitting curves under different I_{DC}.

I_{DC}(A)	0	2	4	6	8	10	12	14	16	18	20
R^2 (%)	57.5	97.6	99.4	99.4	99.4	99.6	99.6	99.3	99.6	99.6	99.7
$\|e\|$	0.34	0.60	0.42	0.47	0.46	0.40	0.38	0.55	0.42	0.39	0.37

5. Conclusion

The DCMIT technique has been introduced for defect depth quantification by using an enhanced thermal feature (T_P). Results have shown that the T_P from traditional IT can hardly be used to quantify the notch depth. The enhanced T_P from DCMIT can be used to quantify the notch depth up to 6.0 mm. Additionally, a larger I_{DC} contributes to a better quadratic fitting relation between T_P and notch depth. In this work, the best quadratic relation (with R^2 and $\|e\|$ of 99.7% and 0.37) is achieved when I_{DC} is 20 A.

Future work will focus on using area- or pattern-based features to quantify surface-breaking cracks with different geometric parameters. Furthermore, comparison studies with other NDT techniques, e.g., ultrasonic testing, eddy current testing, magnetic flux leakage testing, will also be investigated.

Acknowledgements

This work is supported by the National Natural Science Foundation of China (grant numbers 51505308 and 51875576), and the Science and Technology Project of Sichuan Province (grant numbers 2018GZDZX0018 and 2018JY0393).

References

[1] J. A. Davenport, Intergranular corrosion and stress corrosion cracking of sensitised AA5182, Materials Science Forum 519-521 (2006) 641-646.
[2] H. A. Kishawy, H. A. Gabbar, Review of pipeline integrity management practices, Int. J. Pres. Ves. Pip. 87 (2010) 373-380.

[3] H. C. Ma, Z. Y. Liu, C. W. Du, H. R. Wang, X. G. Li, D. W. Zhang, Z. Y. Cui, Stress corrosion cracking of E690 steel as a welded joint in a simulated marine atmosphere containing sulphur dioxide, Corros. Sci. 100 (2015) 627-641.
[4] R. Martínez-Palou, M. de Lourdes Mosqueira, B. Zapata-Rendón, E. Mar-Juárez, C. Bernal-Huicochea, J. de la Cruz Clavel-López, J. Aburto, Transportation of heavy and extra-heavy crude oil by pipeline: A review, J. Petrol. Sci. Eng. 75 (2011) 274-282.
[5] P. Scott, A review of irradiation assisted stress corrosion cracking, J. Nucl. Mater. 211 (1994) 101-122.
[6] M. Rogante, P. Battistella, F. Cesari, Hydrogen interaction and stress-corrosion in hydrocarbon storage vessel and pipeline weldings, Int. J. Hydrogen. Energ. 31 (2006) 597-601.
[7] R. S. Edwards, S. Dixon, X. Jian, Depth gauging of defects using low frequency wideband Rayleigh waves, Ultrasonics 44 (2006) 93-98.
[8] F. Hernandez-Valle, A. R. Clough, R. S. Edwards, Stress corrosion cracking detection using non-contact ultrasonic techniques, Corros. Sci. 78 (2014) 335-342.
[9] P. A. Petcher, S. Dixon, Parabola detection using matched filtering for ultrasound B-scans, Ultrasonics 52 (2012) 138-144.
[10] M. H. Rosli, R. S. Edwards, Y. Fan, In-plane and out-of-plane measurements of Rayleigh waves using EMATs for characterising surface cracks, NDT & E Int. 49 (2012) 1-9.
[11] D. T. Zeitvogel, K. H. Matlack, J. Y. Kim, L. J. Jacobs, P. M. Singh, J. Qu, Characterization of stress corrosion cracking in carbon steel using nonlinear Rayleigh surface waves, NDT & E Int. 62 (2014) 144-152.
[12] L. Babout, T. J. Marrow, D. Engelberg, P. J. Withers, X-ray microtomographic observation of intergranular stress corrosion cracking in sensitised austenitic stainless steel, Mater. Sci. Tech-Lond 22 (2006) 1068-1075.
[13] D. A. Horner, B. J. Connolly, S. Zhou, L. Crocker, A. Turnbull, Novel images of the evolution of stress corrosion cracks from corrosion pits, Corros. Sci. 53 (2011) 3466–3485.
[14] H. Shaikh, N. Sivaibharasi, B. Sasi, T. Anita, R. Amirthalingam, B. P. C. Rao, T. Jayakumar, H. S. Khatak, B. Raj, Use of eddy current testing method in detection and evaluation of sensitisation and intergranular corrosion in austenitic stainless steels, Corros. Sci. 48 (2006) 1462-1482.
[15] G. Y. Tian, A. Sophian, Reduction of lift-off effects for pulsed eddy current NDT, NDT & E Int. 38 (2005) 319-324.
[16] N. Yusa, S. Perrin, K. Mizuno, Z. Chen, K. Miya, Eddy current inspection of closed fatigue and stress corrosion cracks, Meas. Sci. Technol. 18 (2007) 3403-3408.
[17] A. M. Lewis, D. H. Michael, M. C. Lugg, R. Collins, Thin-skin electromagnetic fields around surface-breaking cracks in metals, J. Appl. Phys 64 (1988) 3777-3784.
[18] R. Letessier, R. W. Coade, B. Geneve, Sizing of cracks using the alternating current field measurement technique, Int. J. Pres. Ves. Pip. 79 (2002) 549-554.
[19] H. Rowshandel, G. L. Nicholson, J. L. Shen, C. L. Davis, Characterisation of clustered cracks using an ACFM sensor and application of an artificial neural network, NDT & E Int. 98 (2018) 80-88.
[20] X. Yuan, W. Li, G. Chen, X. Yin, W. Jiang, J. Zhao, J. Ge, Inspection of both inner and outer cracks in aluminum tubes using double frequency circumferential current field testing method, Mech. Syst. Signal Process. 127 (2019) 16-34.
[21] J. Wu, Y. Yang, E. Li, Z. Deng, Y. Kang, C. Tang, A. I. Sunny, A High-Sensitivity MFL Method for Tiny Cracks in Bearing Rings, IEEE T. Magn. 54 (2018) 1-8.
[22] B. Gao, P. Lu, W. L. Woo, G. Y. Tian, Y. Zhu, M. Johnston, Variational bayesian sub-group adaptive sparse component extraction for diagnostic imaging system, IEEE T. Ind. Electron. 65 (2018) 8142-8152.
[23] D. P. Almond, B. Weekes, T. Li, S. G. Pickering, E. Kostson, J. Wilson, G. Y. Tian, S. Dixon, S. Burrows, Thermographic techniques for the detection of cracks in metallic components, Insight-Non-Destructive Testing and Condition Monitoring 53 (2011) 614-620.

[24] X. Huang, C.Yin, S. Dadras, Y. Cheng, L. Bai, Adaptive rapid defect identification in ECPT based on K-means and automatic segmentation algorithm. J. Ambient Intell. Hum. Comput. (2017), 1-18.
[25] Y. He, B. Du, S. Huang, Non-contact Electromagnetic Induction Excited Infrared Thermography for Photovoltaic Cells and Modules Inspection, IEEE T. Ind. Inform. 14 (2018) 5585-5593.
[26] K. Li, G. Y. Tian, L. Cheng, A. Yin, W. Cao, S. Crichton, State detection of bond wires in IGBT modules using eddy current pulsed thermography, IEEE T. Power Electr. 29 (2014) 5000-5009.
[27] J. Wilson, G. Y. Tian, I. Mukriz, D. Almond, PEC thermography for imaging multiple cracks from rolling contact fatigue, NDT & E Int. 44 (2011) 505-512.
[28] H. Zhang, S. Sfarra, A. Osman, F. Sarasini, U. Netzelmann, S. Perilli, C. Ibarra-Castanedo, X. P. Maldague, Eddy current pulsed thermography for ballistic impact evaluation in basalt-carbon hybrid composite panels, Appl. Optics 57 (2018) 74-81.
[29] B. Oswald-Tranta, M. Sorger, Localizing surface cracks with inductive thermographical inspection: from measurement to image processing, Quant. Infr. Therm. J. 8 (2011) 149-164.
[30] B. Oswald-Tranta, Induction Thermography for Surface Crack Detection and Depth Determination, Appl. Sci. 8 (2018) 257.
[31] B. Oswald-Tranta, Lock-in inductive thermography for surface crack detection, Proc. SPIE, Thermosense: Thermal Infrared Applications XL 10661 (2018) 106610U.
[32] Y. Wang, B. Gao, W. L. Woo, G. Y. Tian, X. Maldague, L. Zheng, Z. Guo, Y. Zhu, Thermal Pattern Contrast Diagnostic of Micro Cracks with Induction Thermography for Aircraft Braking Components, IEEE T. Ind. Inform. 14 (2018) 5563-5574.
[33] C. Xu, X. Gong, W. Zhang, G. Chen, An investigation on eddy current pulsed thermography to detect surface cracks on the tungsten carbide matrix of polycrystalline diamond compact bit, Appl. Sci. 7 (2017) 429.
[34] Y. Wang, X. Gao, U. Netzelmann, Detection of surface cracks in metals under coatings by induction thermography, In Proc. of the 14th quantitative infrared thermography conference, Berlin, (2018) 602-611.
[35] P. Jäckel, U. Netzelmann, The influence of external magnetic fields on crack contrast in magnetic steel detected by induction thermography, Quant. Infr. Therm. J. 10 (2013) 237-247.
[36] J. Wu, J. Zhu, H. Xia, C. Liu, X. Huang, G. Y. Tian, DC-biased Magnetization Based Eddy Current Thermography for Subsurface Defect Detection, IEEE T. Ind. Inform. 15 (2019), 6252-6259.
[37] H. S. Carslaw, J. C. Jaeger, Conduction of heat in solids, Oxford Science Publications, Oxford, 1959.
[38] G. Bertotti, Hysteresis in magnetism: for physicists, materials scientists, and engineers, Academic Press, San Diego, 1998, pp. 25 & 428.
[39] J. Vrana, M. Goldammer, K. Bailey, M. Rothenfusser, W. Arnold, Induction and conduction thermography: optimizing the electromagnetic excitation towards application, In AIP Conference Proc. 1096 (2009) 518-525.
[40] J. Zhu, Q. Min, J. Wu, G. Y. Tian, Probability of Detection for Eddy Current Pulsed Thermography of Angular Defect Quantification, IEEE T. Ind. Inform. 14 (2018) 5658-5666.
[41] B. D. Cullity, C. D. Graham, Introduction to magnetic materials, John Wiley & Sons, New Jersey, 2011.
[42] S. Ishikawa, S. Yanase, Y. Okazaki, AC magnetic properties of electrical steel sheet under two-dimensional dc-biased magnetization, IEEE T. Magn. 48 (2012) 1413-1416.
[43] S. Ke, H. Zhang, Z. Ni, D. Ye, G. Zhang, & L. Su., Common Steel Magnetic Characteristics Quick Reference, China Machine Press, Beijing, 2003.
[44] X. P. Maldague, Nondestructive evaluation of materials by infrared thermography, Springer Science & Business Media, New York, 1993.